The Astrophysical Journal, 885:112 (11pp), 2019 November 10 https://doi.org/10.3847/1538-4357/ab46b3

Application of the Thermal Wind Model to Absorption Features in the Black Hole X-Ray Binary H1743–322

Megumi Shidatsu[1] and Chris Done[2]
[1] Department of Physics, Ehime University, Matsuyama 790-8577, Japan; megumi.shidatsu@riken.jp
[2] Department of Physics, University of Durham, South Road, Durham, DH1 3LE, UK

Received 2019 June 6; revised 2019 September 17; accepted 2019 September 20; published 2019 November 6

Abstract

High inclination black hole X-ray binaries exhibit blueshifted ionized absorption lines from disk winds, whose launching mechanism is still in debate. The lines are predominantly observed in the high/soft state and disappear in the low/hard state, anticorrelated with the jet. We have tested if the thermal winds, which are driven by the irradiation of the outer disk by the X-rays from the inner disk, can explain these observed properties or whether we need a magnetic switch between jet and wind. We use analytic thermal-radiative wind models to predict the column density, ionization parameter, and velocity of the wind given the broadband continuum shape and luminosity determined from the *Rossi X-ray Timing Explorer* (*RXTE*) monitoring. We use these to simulate the detailed photoionized absorption features predicted at epochs where there are *Chandra* high-resolution spectra. These include low/hard, high/soft, and very high states. The model was found to well reproduce the observed lines in the high/soft state, and it also successfully predicts their disappearance in the low/hard state. However, the simplest version of the thermal wind model also predicts that there should be strong features observed in the very high state, which are not seen in the data. Nonetheless, we show this is consistent with thermal winds when we include self-shielding by the irradiated inner disk atmosphere. These results indicate that the evolution of observed wind properties in different states during outbursts in H1743−322 can be explained by the thermal wind model and does not require magnetic driving.

Key words: accretion, accretion disks – black hole physics – line: profiles – X-rays: individual (H1743)

1. Introduction

Disk winds have been observed in several black hole X-ray binaries (BHXBs) as blueshifted, highly ionized, absorption lines, especially H- or He-like iron-K lines, on the X-ray continuum spectra (e.g., Kotani et al. 2000; Ueda et al. 2001; Miller et al. 2006a; Kubota et al. 2007; Miller et al. 2008; Díaz Trigo et al. 2014; Hori et al. 2018). They are only seen in high-inclination systems, suggesting that the winds have an equatorial structure, extending along the disk plane with a small solid angle (Ponti et al. 2012). The observed winds have state dependence; the absorption lines are predominantly seen in the high/soft state and tend to be more ionized with spectral hardening (Díaz Trigo et al. 2014; Hori et al. 2018), and finally disappear in the low/hard state (Miller et al. 2008; Neilsen & Lee 2019; Miller et al. 2012; Ponti et al. 2012).

What drives the winds in BHXBs is a longstanding question. Radiation pressure by Compton scattering can drive winds when it overcomes the gravity of the central black hole. This mechanism, by definition, only works above the Eddington luminosity ($L_{\rm Edd}$), but most of the systems are well below $L_{\rm Edd}$, hence this continuum-radiation-pressure driven wind is unlikely to explain the majority of the disk winds seen in BHXBs. Radiation pressure on bound-free or line transitions can launch a wind below $L_{\rm Edd}$, giving a plausible mechanism for some winds in active galactic nuclei (Proga et al. 2000; Nomura et al. 2016), but it is again unlikely to work in BHXBs because their much higher temperature disks mean that the strong UV absorption species are completely ionized (Proga & Kallman 2002).

Instead, a promising launching mechanism of winds in BHXBs is thermal driving. The outer disk regions are irradiated by the strong X-rays emitted from the inner disk region. Gas in the disk photosphere is then heated to the Compton temperature, $T_{\rm IC}$, where Compton up and down scattering is balanced. This temperature is determined by the shape of the spectral energy distribution, as

$$T_{\rm IC} = \frac{\int_0^\infty h\nu L_\nu d\nu}{4k\int_0^\infty L_\nu d\nu}, \tag{1}$$

where h is the Planck constant, and k is the Boltzmann constant (see, e.g., Begelman et al. 1983; Done 2010). Its typical value for BHXBs is $\sim 10^7$ K in the high/soft state. This gas can escape from the disk when its kinetic energy overcomes the local gravitational energy. This gives an estimate for the wind launching radius, $R_{\rm IC} \sim GM_{\rm BH}\mu/kT_{\rm IC}$, where $\mu \sim 0.6m_p$ is the mean particle mass in the wind (Begelman et al. 1983; Woods et al. 1996). If the outer disk radius $R_{\rm out}$ is smaller than $R_{\rm IC}$, the illuminated gas is kept bound on the disks, forming a static ionized atmosphere above the disks, which indeed has been observed in many short-period (mainly neutron star) X-ray binaries (Díaz Trigo & Boirin 2013), whereas winds are observed only in systems with big disks (Díaz Trigo & Boirin 2016).

The final mechanism, magnetic driving, has drawn growing interest since the discovery of a peculiar wind in GRO J1655−40 (Miller et al. 2006a, 2008; Fukumura et al. 2017), in which the wind launching radius calculated from the absorption features was much smaller than $R_{\rm IC}$. This idea, that the magnetic fields powers the winds, also led attempts to explain the observed state dependence of the wind properties as an anticorrelation with the jet, so that the same magnetic field reconfigures to power the jet in the low/hard state and the wind in the high/soft state (Fukumura et al. 2014). However, their launching site is very different: winds are generally launched in the outer disk regions, whereas jets are believed to be powered in the innermost regions of the disk, hence it is not likely that they are really associated via the same magnetic fields. Also, recent studies suggests that the peculiar wind in GRO J1655−40 may be explained by a Compton-thick, thermal- (plus continuum-radiation-pressure) driven wind (Uttley & Klein-Wolt 2015; Neilsen et al. 2016; Shidatsu et al. 2016).

Given that thermal winds are relatively well understood theoretically (Begelman et al. 1983; Woods et al. 1996; Higginbottom et al. 2014), compared with the magnetic winds, one possible approach would be to study the extent to which the thermal winds can describe the observed absorption features and its state dependence, and then explore how much room remains to invoke magnetic winds. Done et al. (2017, hereafter D18) provided a predictive thermal wind model, which can derive the basic wind parameters including the column density and the ionization parameter. They set up a simplified spectral model, where the continuum depends only on L/L_{Edd}, such that it was dominated by a disk with $L \propto T^4$ in the high/soft state, switching to a power law for the low/hard state at $L/L_{\mathrm{Edd}} = 0.02$. They concluded that the resultant thermal (and thermal-radiative) wind properties could explain most (and perhaps all) of the currently available data. However, the actual spectral evolution in BHXBs is more complex, and not determined by luminosity alone. The high luminosity states are not always dominated by the disk emission as assumed in D18, but can have a more substantial soft Compton tail (a very high state). Also, the transition to the low/hard state is not at a fixed luminosity, as displayed by the hysteresis seen in the hardness-intensity diagram. These different spectral energy distribution (SED)-Luminosity behaviors will change the predicted wind properties, as the thermal winds are very sensitive to the shape of the continuum spectrum as well as its luminosity.

Here, we instead use the actual X-ray data of the BHXB H1743−322 taken in monitoring observations with *RXTE* and *Swift*, to accurately determine the continuum spectral shape and luminosity throughout the outbursts. We then predict the thermal wind parameters (column density, ionization state, and velocity) appropriate for each spectrum using the D18 model to predict how the thermal winds evolve across a real outburst. There are also several *Chandra* high-resolution spectra taken in different states, including the high/soft state where the wind features were visible, and the low/hard and very high states where they were not significantly detected. We use photo-ionization models to compare the detailed predictions of the thermal wind model with the high-resolution spectra, and find that they are a good match to the observations. We conclude that these winds are most likely thermally driven rather than powered by magnetic fields.

2. System Parameters and Long-term X-Ray Properties of H1743−322

We first summarize the X-ray and binary system properties of H1743−322. This is one of the systems in which winds have been detected (see e.g., Ponti et al. 2012).

This source has exhibited many outbursts which have been extensively observed at various wavelengths, especially with the *Rossi X-ray Timing Explorer* (*RXTE*) and *Swift*. These also provide daily broadband X-ray monitoring data covering the entire outburst periods. Figure 1 presents X-ray light curves in 1.5–12 keV from the *RXTE*/All Sky Monitor (ASM) and in 15–50 keV from the *Swift*/Burst Alert Telescope (BAT). The ASM hardness ratio (HR) between 5–12 keV and 3–5 keV is also shown as the lower panel in Figure 1, with state transitions to the high/soft state indicated by HR $\lesssim 1$.

Chandra carried out high-resolution spectroscopy several times in these outbursts as listed in Table 1. These sample different spectral state and luminosities. Observations with statistics that are too low are omitted. As given in this table, we hereafter call these *Chandra* epochs Soft1, Soft2, VHS, Hard1, and Hard2. The three sequential observations in 2015 (Hard2), where the luminosity and SED profile do not differ significantly, are combined to obtain high-resolution spectrum in the low/hard state at a relatively low luminosity, although *RXTE* already ended its operation and the broadband continuum data are unavailable. Hence, we estimate the HR and luminosity by matching to *RXTE* data at similar 3–7 keV continuum shape and luminosity. The H-like and He-like Fe Kα absorption lines are clearly detected only in the high/soft state (Soft1 and 2), whereas no significant lines were detected in the other epochs (Miller et al. 2006b, 2012).

The inclination angle and the distance of H1743−322 were constrained by Steiner et al. (2012) from the trajectory of ballistic jets as $75° \pm 3°$ and 8.5 ± 0.8 kpc, respectively. The high inclination angle is supported by the fact that the source shows absorption dips in its X-ray light curves and ionized absorption lines from winds in its spectra. Short-term variability properties also imply a high inclination angle; the source shows a somewhat stronger low frequency QPOs in the low/hard state than low inclination BHXBs, as expected if the QPO is a geometric effect such as Lense–Thirring precession (Ingram et al. 2009). Steiner et al. (2012) estimated the black hole mass as $\sim 7 M_{\odot}$ from disk continuum fits with a relativistic accretion disk emission model (assuming spin parameter, $a_* = 0.2$).

The outer disk radius R_{out}, is poorly known, but this is a critical parameter for calculation of the thermal winds. We estimate this from comparison of the frequency of outbursts to disk instability calculations. The multiple outbursts suggest that the mass-transfer rate from the companion star is close to the critical mass accretion rate where the hydrogen ionization instability is triggered (Coriat et al. 2012). GX 339−4 is similarly a system which shows frequent outbursts, so we assume that the orbital period of H1743−322 is similar to that of GX 339−4 (∼40 hr). Thus the disk would similarly extend to a few tens of percent of its Roche lobe, giving an estimate for $R_{\mathrm{out}} \sim 3 \times 10^{11}$ cm, but this must be uncertain by at least a factor of two in either direction. This disk size is likely the smallest among the BHXBs in which winds have been detected (Ponti et al. 2012), hence it is the simplest to model (see also Tomaru et al. 2019).

We note that D18 used different system parameters for this source, with a black hole mass of $10 M_{\odot}$ and spin of 0.5 at a distance of 5 kpc. Most importantly, they assumed $R_{\mathrm{out}} = 3.7 \times 10^{12}$ cm, almost an order of magnitude larger than here. The predicted column density in the wind material is $\propto \log R_{\mathrm{out}}/R_{\mathrm{wind}}$ (where R_{wind} is the wind launching radius), so typically our columns will be a factor of ∼1.8 smaller for a given L/L_{Edd}.

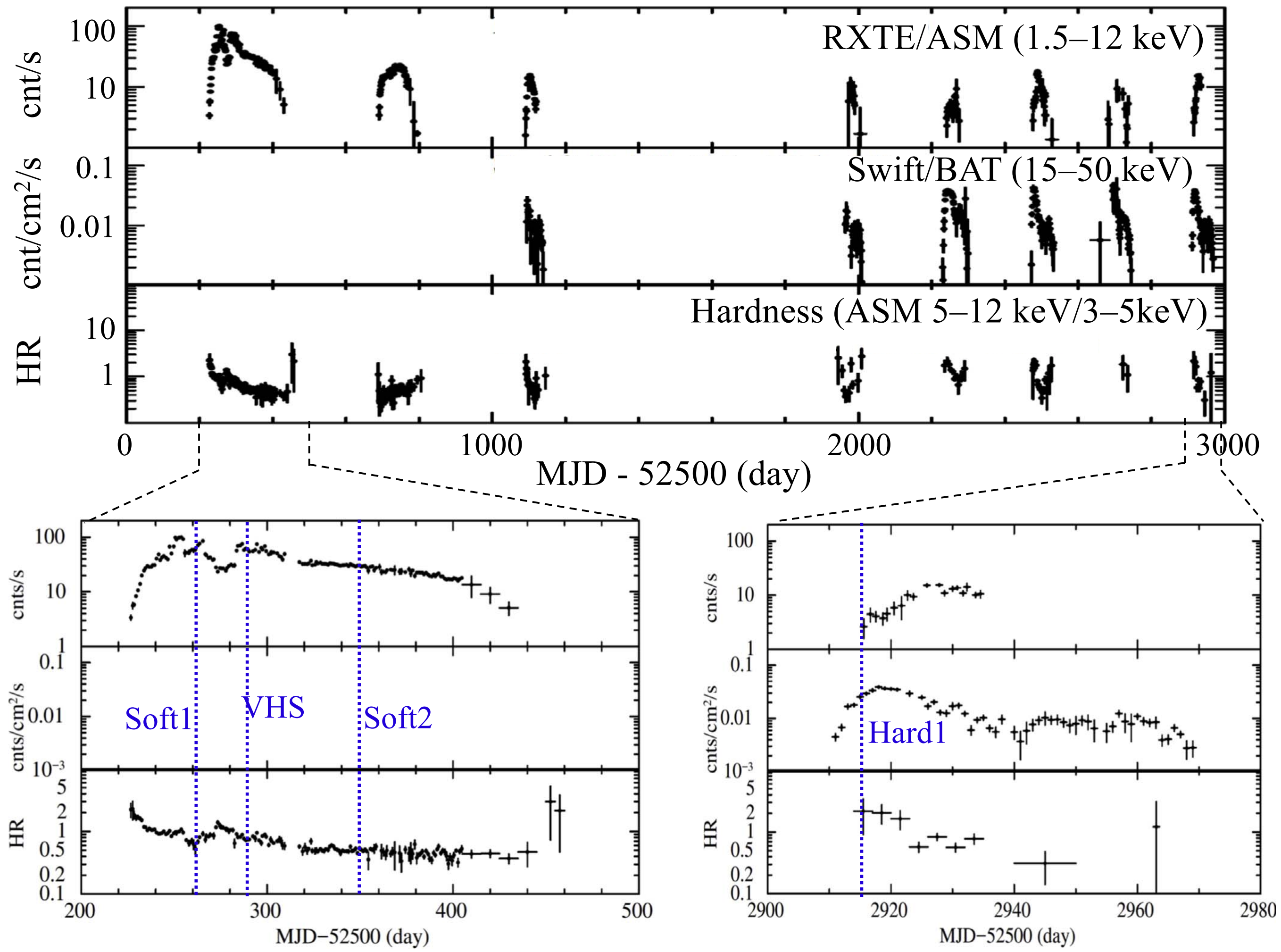

Figure 1. Long-term light curves and hardness ratio of H1743−322 until 2011. The bottom panels are enlarged views of the top panel. The *Chandra* observations before 2011 considered in this work are indicated in blue dotted lines. At Hard2 in 2015, the *Swift*/BAT count rate was ∼0.01 counts cm^{-2} s^{-1}.

Table 1
List of *Chandra*/HETGS Observations Considered in this Work

Epoch	OBSID	Date	State	Lines?
Soft1	3803	2003 May 1–2	high/soft	yes
VHS	3804	2003 May 28	very high	no
Soft2	3806	2003 Jul 30–31	high/soft	yes
Hard1	11048	2010 Aug 8–9	low/hard	no
Hard2[a]	16738	2015 Jul 11	low/hard	no
Hard2[a]	17679	2015 Jul 12	low/hard	no
Hard2[a]	17680	2015 Jul 13	low/hard	no

Note.
[a] The luminosities and SED profiles are almost the same in the three observations and their spectra are coadded to improve statistics in Section 5.

3. Modeling Continuum X-Ray Spectra

We produced broadband X-ray spectra corresponding to each pointed *RXTE*/PCA observation of H 1743−322. These were extended to higher energies using *RXTE*/HEXTE (up to 2010) or *Swift*/BAT (after 2010).

The *RXTE* data were reduced in the standard manner described in the *RXTE* cookbook, by using HEAsoft version 6.19 and the Calibration Database (CALDB) downloaded in 2016 December. We extracted the PCA spectra from the "Standard 2" data of the Proportional Counter Array 2 (PCA2) and the HEXTE spectra from Clusters A and B data. To obtain hard X-ray spectra after 2009 December, when the *RXTE*/HEXTE stopped rocking between the on-source and off-source positions, we used the *Swift*/BAT survey data taken on the same day as *RXTE*/PCA data. The BAT survey data were downloaded from the HEADAS archive[3] and processed with the ftool `batsurvey` referring to the latest *Swift* CALDB as of 2016 December. The spectra and their response files were generated from the individual continuous scans using the script `make_survey_pha`. We chose the scan with the longest exposure if multiple scans were present. In this way, we obtained ∼500 simultaneous broadband X-ray spectra of H1743−322, covering 8 outbursts from 2003 March to 2011 April.

Figure 2 presents the resulting broadband continuua corresponding to the *Chandra* high-resolution data sets in Soft1, Soft2, VHS, and Hard1. In Figure 2(d) we also present the *Chandra* HEG spectrum at Hard2 and a corresponding *Swift*/BAT spectrum taken on 2015 July 12. The Soft1 and Soft2 spectra are both high/soft state, dominated by the disk blackbody component, especially Soft2 which has an extremely weak hard tail. The VHS spectrum, taken at the highest

---

[3] https://heasarc.gsfc.nasa.gov/FTP/swift/data/obs/

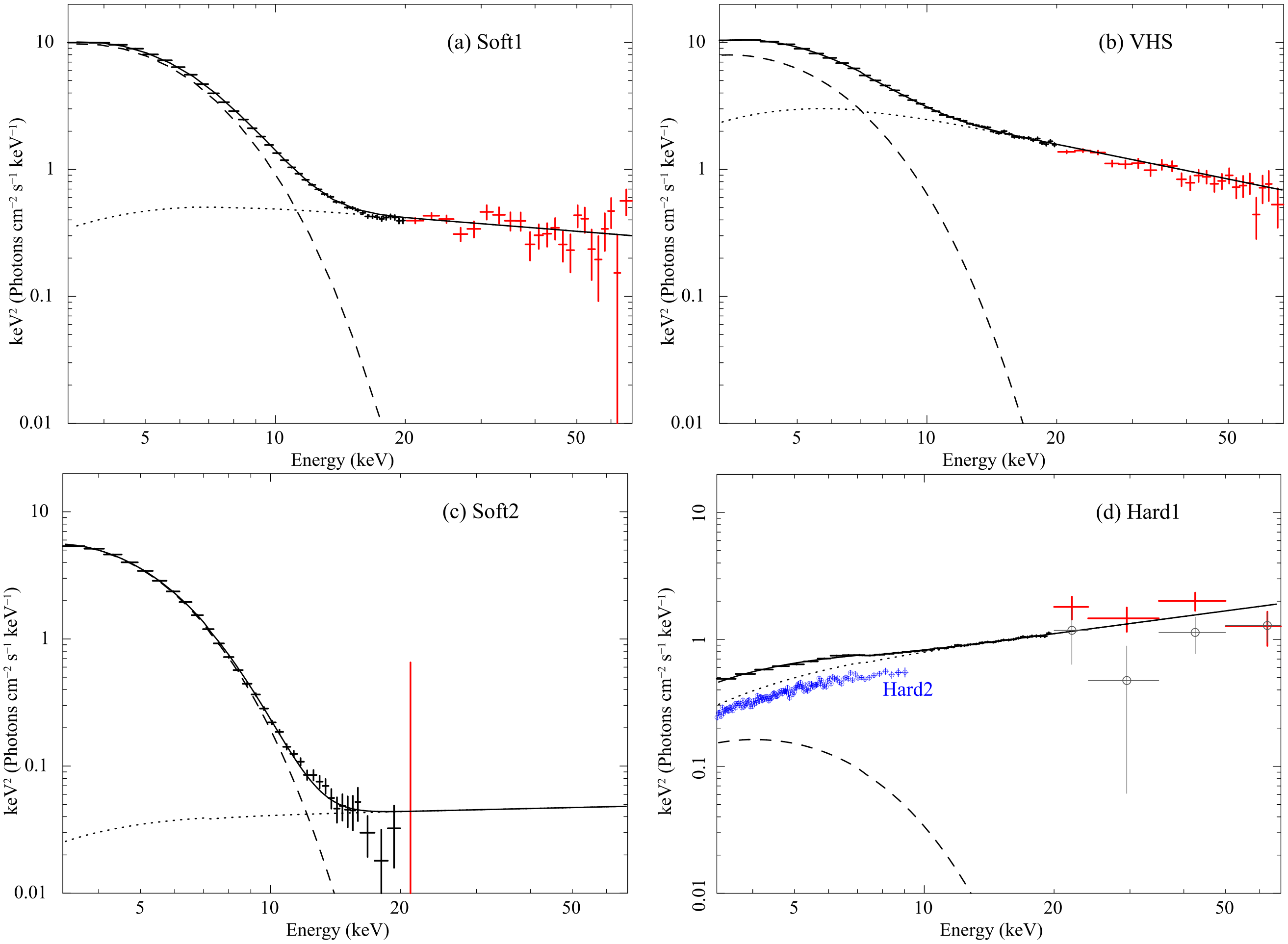

Figure 2. Broadband continuum spectra of H1743−322 at the four *Chandra* epochs in 2003–2010, with their best-fit `tbabs*simpl*diskbb` models. The *RXTE*/PCA data are shown in black, and the *RXTE*/HEXTE Cluster-A (in panel a–c) and *Swift*/BAT data (in panel d) in red. The HEXTE Cluster-B data are omitted in the panel (a–c) for illustrative purposes. In panel (d), the *Chandra* HEG spectrum and a *Swift*/BAT spectrum at Hard2 are also plotted with blue and gray circles, respectively, for comparison with Hard1 (see Section 5 for the details of the *Chandra* data).

luminosity among the four epochs, can be approximated by a steep power-law model, indicating that the source was in the very high state. Hard1 shows a typical low/hard state spectrum with a hard power-law-shaped profile. Hard2 has a slightly harder and dimmer continuum in the 3–9 keV range, and is characterized by a power-law model with a photon index of ∼1.33.

We analyzed the individual broadband X-ray continuum spectra in XSPEC version 12.9.0n, with a model consisting of the multi-color disk blackbody emission (`diskbb`: Mitsuda et al. 1984) and its Comptonization component (`simpl`: Steiner et al. 2009). The `simpl` Comptonization model convolves a fraction of an input spectrum into a power law, using the photon index (Γ) and the fraction of the total input X-ray flux that is scattered (F_{scat}). We accounted for interstellar absorption by multiplying the resulting `simpl*diskbb` model by `TBabs` (Wilms et al. 2000) with fixed $N_H = 1.6 \times 10^{22}$ cm^{-2} (Capitanio et al. 2009). We checked that allowing this column to be free gives consistent results, with most of the observations giving values within $\sim 5 \times 10^{21}$ cm^{-2} and $\sim 3 \times 10^{22}$ cm^{-2}. However, some spectra around the state transitions gave more discrepant results, but these are most likely due to our continuum model being too simple for these complex spectra rather than to any additional neutral column intrinsic to the source. We checked that the slight change in best-fit spectral parameters did not affect the overall trends in wind parameters in Section 4 and the XSTAR simulation results in Section 5.

We extend the energy range used to calculate the model in XSPEC to 0.1–500 keV, to avoid systematic errors in the `simpl` convolution at the upper/lower energy edges of the data. We discarded the data with 3–10 keV unabsorbed fluxes below 9×10^{-11} erg cm^{-2} s^{-1} (which corresponds to the Eddington ratio in 0.01–100 keV of $L/L_{\mathrm{Edd}} \sim 0.002$) because the Galactic ridge emission was found to contaminate strongly and its iron-K emission lines are clearly seen in the PCA spectra. The remaining 435 spectra was used in the following analysis.

The continuum spectra are well reproduced with this model and we used the resulting SED from 0.01–100 keV to calculate the Compton temperature, T_{IC}, for each individual observation. Figure 2 shows these model fits for the broadband continuum at the 4 *Chandra* epochs before 2011, with the individual components shown separately. Model parameters and T_{IC} are shown in Table 2.

The blackbody seen in the low/hard state spectrum in Hard1 is quite hot and dim. Its temperature (T_{in}) is higher than that in the 2003 epochs, which is inconsistent with that expected decrease in disk temperature from high/soft state to the low/hard state. When we fit the two data simultaneously linking

Table 2

Best-fit Parameters of the Continuum Spectra at the Individual *Chandra* Epochs, and their Wind Parameters Obtained with the D18 Model

Epoch		Soft1	VHS	Soft2	Hard1
State		High/Soft	Very High	High/Soft	Low/Hard
Best-fit continuum parameters					
`TBabs`	$N_{\rm H}$ (10^{22} cm^{-2})	1.6 (fixed)	1.6 (fixed)	1.6 (fixed)	1.6 (fixed)
`simpl`	$F_{\rm scat}$	$2.4^{+0.1}_{-0.2} \times 10^{-2}$	0.170 ± 0.006	$3^{+3}_{-1} \times 10^{-3}$	$0.652^{+0.020}_{-0.001}$
	Γ	2.27 ± 0.06	2.69 ± 0.03	1.9 ± 0.6	1.55 ± 0.03
`diskbb`	$T_{\rm in}$ (keV)	1.221 ± 0.002	1.189 ± 0.006	$1.026^{+0.004}_{-0.005}$	$1.49^{+0.02}_{-0.03}$
	norm	$(8.17 \pm 0.08) \times 10^2$	$(8.8 \pm 0.2) \times 10^2$	$(9.9 \pm 0.2) \times 10^2$	15.95 ± 0.03
	L (10^{38} erg s^{-1})[a]	3.6	4.7	2.1	0.67
	$L/L_{\rm Edd}$[b]	0.33	0.39	0.20	0.062
	L_0 (10^{38} erg s^{-1})[c]	3.5	3.7	2.1	0.2
	$T_{\rm IC}$ (10^8 K)	0.11	0.16	0.07	1.0
Wind parameters					
	n_0 (10^{12} cm^{-3})	1.0	2.9	0.1	2.1
	$R_{\rm wind}$ (10^{10} cm)	6.6	4.0	13	1.3
	$N_{\rm H}$ (10^{22} cm^{-2})	6.7	12	1.5	2.6
	ξ (10^4 erg cm s^{-1})	8.1	8.5	10	21
	$v_{\rm wind}$ (10^2 km s^{-1})	3.9	4.7	3.1	11

Notes.

[a] Unabsorbed 0.01–100 keV luminosity, assuming a distance of 8.5 kpc.

[b] A black hole mass of 7 $M_\odot$ is assumed (i.e., $1L_{\rm Edd} = 1.\ 1 \times 10^{39}$ ergs s^{-1}).

[c] Unabsorbed 0.0136–13.6 keV luminosity, which is used in XSTAR simulations.

$N_{\rm H}$ and allowing it to vary, $T_{\rm in}$ in Hard1 decreases to $\approx$1.2 keV but still comparable to that of the 2003 epochs. We suggest that the thermal component in Hard1 likely does not represent the true disk component, but rather it is compensating for an additional soft Comptonization component seen in the bright low/hard state (e.g., Makishima et al. 2008; Yamada et al. 2013; Shidatsu et al. 2014; Mahmoud et al. 2019). We note that in the low/hard state the spectral shape below $\sim$1 keV does not affect the derived wind parameters as $T_{\rm IC}$ is more sensitive to the hard tail than to a weak disk component. We also fit the low/hard state spectrum with a single power-law model, but the resultant values of L, $T_{\rm IC}$, and wind parameters calculated in Section 4 only changed by 10%–20% from the values in Table 2, which does not affect the results of the XSTAR simulation in Section 5.

4. Overall Properties of Thermal Wind

Now that we have Compton temperatures in each *RXTE* pointed observation, we can apply the D18 model to calculate the basic observable quantities of the thermal wind from the assumed system parameters of H1743−322, and hence study the predicted evolution of wind properties during the specific outbursts seen here.

D18 uses the analytic approximation of the wind mass-loss rate $\dot{M}_{\rm out}$ as a function of L, derived by Begelman et al. (1983), with two-dimensional density structure based on the results of the hydrodynamic simulations of Woods et al. (1996). Assuming a simple density structure, $n(R, i) \propto R^{-2}(1 - \cos i)$, the column density of a thermal wind is derived as

$$N_{\rm H}(i) = \frac{\dot{M}(1 - \cos i)}{4\pi R_{\rm wind} v_{\rm wind} m_{\rm I}}, \tag{2}$$

and the ionization parameter as

$$\xi(i) = \frac{L}{nR_{\rm wind}^2} = \frac{4\pi L v_{\rm wind} m_{\rm I}}{\dot{M}(1 - \cos i)}, \tag{3}$$

where $v_{\rm wind}$ is the wind velocity, for which the mass-loss averaged sound speed is adopted, and $m_{\rm I}$ is the mean ion mass for one electron ($m_{\rm I} \sim 2\mu$).

The actual wind launching radius $R_{\rm wind}$ is determined from that derived from the Compton temperature $R_{\rm IC}$. When the luminosity approaches the Eddington luminosity $L_{\rm Edd}$, the radiation pressure reduces the effective gravity, leading a decrease in the wind launching radius. To consider this effect, we adopt a simple correction of $R_{\rm IC}$, following D18, as

$$\overline{R_{\rm IC}} = R_{\rm IC}\left(1 - \frac{L}{L_{\rm Edd}/\sqrt{2}}\right). \tag{4}$$

We note that this correction is applicable only below $L = L_{\rm Edd}/\sqrt{2}$, so that the radius is a positive value (see also Section 6 for the limitations in the D18 model). The $R_{\rm wind}$ value is given as $R_{\rm wind} = 0.2\overline{R_{\rm IC}}$ for $L \geqslant L_{\rm crit}$, and $R_{\rm wind} = 0.2\overline{R_{\rm IC}} L_{\rm crit}/L$ for $L < L_{\rm crit}$, where the critical luminosity, $L_{\rm crit} \sim 3 \times 10^2 T_{\rm IC}^{-1/2} L_{\rm Edd}$, is defined by the luminosity at which the heating rate is sufficient to raise the gas temperature to $T_{\rm IC}$ at $0.2R_{\rm IC}$ so that it can escape (Begelman et al. 1983). Thus, the basic wind parameters $N_{\rm H}$, ξ, $R_{\rm wind}$, and $v_{\rm wind}$ can be estimated from L and $T_{\rm IC}$ given the assumed system parameters $M_{\rm BH}$, i, and $R_{\rm out}$. Table 2 lists the wind parameters estimated from the D18 model at the *Chandra* epochs for this system.

To understand how the properties of thermal winds change in an outburst, we plotted the three observable parameters, $L_{\rm X}$, $N_{\rm H}$, and ξ with respect to $T_{\rm IC}$ in Figure 3. We also included the hardness versus luminosity diagram, so that we can easily associate these parameters with spectral states. The launch

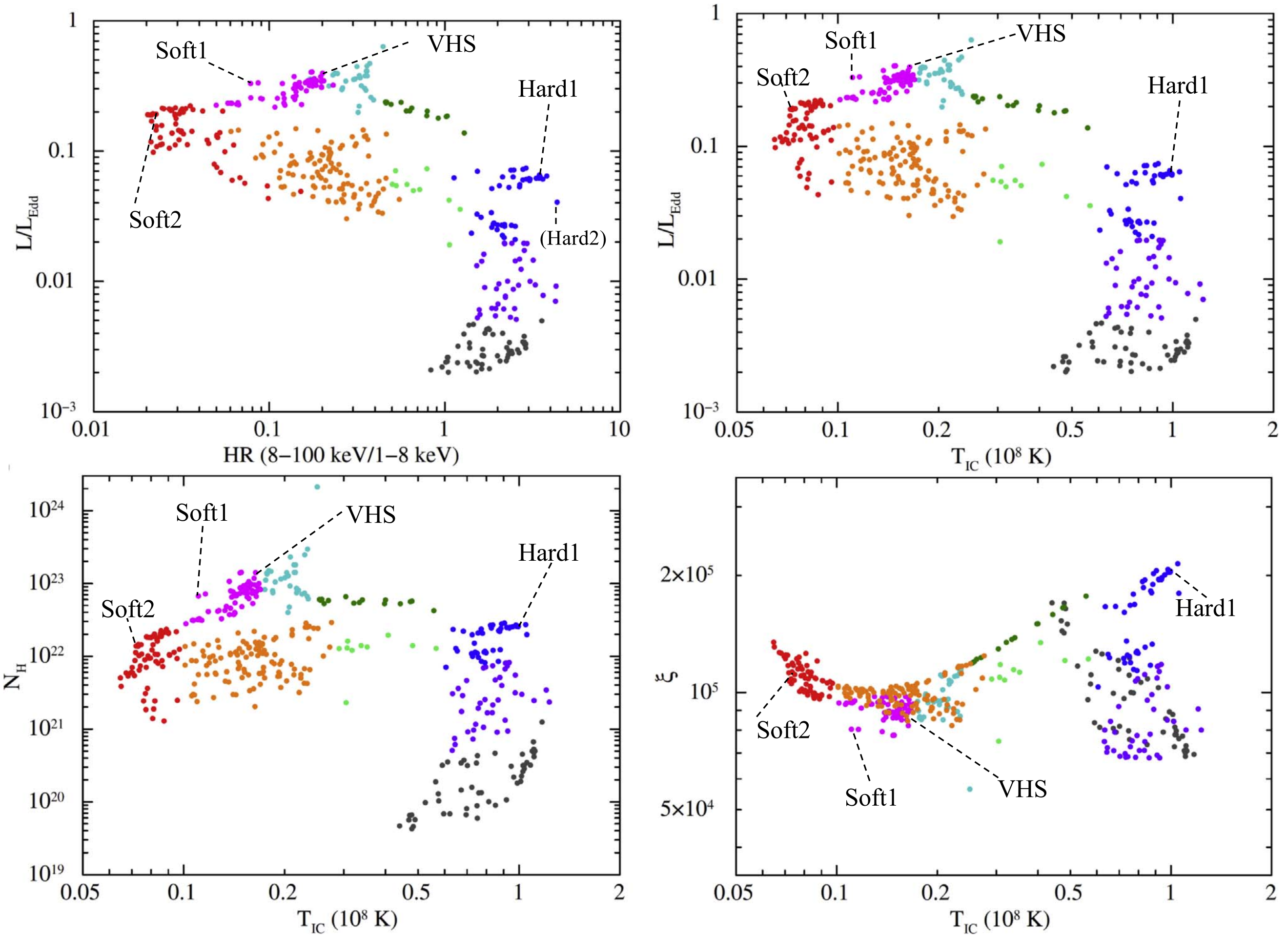

Figure 3. (Upper left) Hardness ratio vs. luminosity diagram, for outbursts of H1743−322 from 2003 to 2011. HRs are calculated from the unabsorbed 1–8 keV and 8–100 keV fluxes, and the luminosity from the unabsorbed 0.01–100 keV flux, all estimated from the best-fit continuum model. The data points are separated into nine groups and shown in different colors so that these could be tracked in the predictions of wind parameters in the other panels. (Upper right) Relation between $T_{\rm IC}$ and $L/L_{\rm Edd}$. (Lower left and right) Evolution of $N_{\rm H}$ and ξ of thermal winds with respect to $T_{\rm IC}$, respectively, predicted by the D18 model. The same color codes as in the upper panels are used. The *Chandra* epochs before 2011 are indicated with dashed lines. The 2015 epoch (Hard2) is also indicated in the top-left panel, by assuming that it is located at the same position as the *RXTE* point with the closest flux and spectral shape in 3–9 keV.

radius of the wind is generally $0.2R_{\rm IC} \propto 1/T_{\rm IC}$, while $v_{\rm wind} \propto T_{\rm IC}^{1/2}$. Hence, $N_{\rm H} \propto LT_{\rm IC}^{1/2}$, while $\xi \propto T_{\rm IC}^{1/2}$. At the highest luminosities above 30%–40% $L_{\rm Edd}$, however, $N_{\rm H}$ and ξ become even larger and lower, respectively, due to the effect of the radiation pressure correction.

Because $T_{\rm IC}$ increases as the X-ray spectrum becomes harder, the $T_{\rm IC}$ versus $L_{\rm X}$ plot (the top-right panel in Figure 3) can be regarded as the hardness-intensity diagram. Indeed, it makes almost the same track as the hardness luminosity diagram (top left in Figure 3) and shows hysteresis; the transition from the low/hard state to the high/soft state occurs at a higher luminosity than the opposite transition. A similar track can be seen in the $T_{\rm IC}$–$N_{\rm H}$ plot, as $N_{\rm H} \propto L_{\rm X} T_{\rm IC}^{1/2}$, so it depends more strongly on $L_{\rm X}$ than spectral hardness. By contrast, the $T_{\rm IC}$–ξ plot exhibits a very different track, as $\xi \propto T_{\rm IC}^{1/2}$ only.

We note that the $T_{\rm IC}$–ξ diagram does not directly indicate the visibility of the Fe K absorption lines, because the ξ value is estimated from the bolometric luminosity and does not incorporate the information on the spectral shape. The hard X-ray fraction in the total luminosity is ∼1 order of magnitude larger in the low/hard state (colored in black, purple, and blue in Figure 3) than in the high/soft state (colored in pink, red, and orange). Hence, the wind is completely ionized during the former state, leading to the absence of the lines, whereas it often produces lines in the latter state, even if the ξ values are not very different (see also Section 6). We incorporate this spectral shape information in the next section.

5. Detailed Photoionized Plasma Simulations

Adopting the wind parameters given in Table 2 as input to the XSTAR photoionization code, we made detailed simulations of the wind absorption features at the *Chandra* epochs. We used XSTAR version 2.41 together with XSTAR2XSPEC, which runs XSTAR simulations multiple times to provide an XSPEC table model of ionized absorption, based on the simulation results. The XSTAR simulations were performed for the individual *Chandra* epochs, using their best-fit continuum models as the input SEDs. Here, the density n_0 at the wind launching radius and the ionizing luminosity, L_0, in 0.0136–13.6 keV used in XSTAR were fixed at the values in Table 2, while ξ, $N_{\rm H}$, and the blueshift (or the line-of-sight velocity $v_{\rm wind}$) were varied. The turbulent velocity was set at 300 km $\rm s^{-1}$ and abundances were set to solar. In these simulations, we assumed that the density of the ionized plasma is constant with respect to radius, although the D18 model adopts the radial dependence as $n(r) = n_0(r/R_{\rm wind})^{-2}$. This is because the simulations never converge when we use the latter dependence, due to technical reasons in XSTAR.[4]

The resultant table model for the individual epochs was added to their best-fit continuum models obtained from the fits to the broadband data (see Section 3) and applied to the *Chandra*/HETGS data at each epoch. We utilized first-order HEG spectra in 3–9 keV and their response files, downloaded from the *Chandra* Transmission Grating Data Archive and Catalog (Huenemoerder et al. 2011). The HEG continuum spectra were found to be somewhat harder than the corresponding *RXTE*/PCA spectra, and significant residuals remain mainly above ∼8 keV. This could be be due to time variability between the *RXTE* and *Chandra* observations, which are not exactly simultaneous, or by spectral distortion by dust scattering halo (Allen et al. 2018), or by a calibration uncertainty in *Chandra* responses. To reduce the discrepancy between the HEG data and the continuum model, we varied $T_{\rm in}$ and normalization of `diskbb` for the high/soft state and Γ and $F_{\rm scat}$ of the `simpl` model for the low/hard state and the very high state, We note that this treatment, which allows the above parameters to be different from those obtained from the *RXTE* (+*Swift*/BAT) data, only slightly changes $T_{\rm IC}$ from the original values and does not affect the wind parameters.

In the following, we show the results of the simulations and demonstrate how they reproduce the data at each epoch.

5.1. High/Soft State (Soft1 and Soft2)

In Figure 4(a), the model obtained from the XSTAR simulation is compared with the *Chandra* spectrum for Soft1. We first fix $N_{\rm H}$, ξ, and the blueshift velocity at the values in Table 2. The observed He-like and H-like Fe lines at 6.7 keV and 7.0 keV, respectively, are well reproduced by the model. By contrast, Figure 4(b), allows the three wind parameters to vary, to find the best-fit description of the data. In this case, the fit quality marginally improved from the case of fixed wind parameters, from $\chi^2/{\rm dof} = 1774/1096$ to $1761/1093$, and $N_{\rm H} = (4 \pm 1) \times 10^{22}$ cm^{-2}, $\xi = 3^{+2}_{-1} \times 10^4$ erg cm s^{-1}, and $v_{\rm wind} = 5 \pm 1 \times 10^2$ km s^{-1} were obtained. This combination gives very similar line equivalent widths as the material is so highly ionized that the decrease in ionization parameter means that less of the iron is completely ionized, so increases the column in Fe XXV and XXVI in such a way as to offset the decrease in overall column density. Whichever combination is chosen, it is clear that the thermal wind model predictions can explain this observation within a factor of ∼2 uncertainties.

The D18 analysis had the observed source $L/L_{\rm Edd} = 0.1$ at Soft1 due to the difference in distance/mass/spin, but assumed limb darkening so that their intrinsic $L/L_{\rm Edd} = 0.3$–0.4, as assumed here from the observed spectrum at these different system parameters. Their estimate for $N_{\rm H} = 8 \times 10^{22}$ cm^{-2} for a source at this luminosity is slightly larger than the $N_{\rm H} = 6.7 \times 10^{22}$ cm^{-2} predicted here due to their larger $R_{\rm out}$.

Figures 5(a) and (b) compare the Soft2 data taken at $L/L_{\rm Edd} = 0.2$ and the corresponding XSTAR absorption model, in the same way as Soft1. At this epoch the source exhibited a much softer SED and had a hard tail ∼10 times weaker than Soft1. Our prediction using the D18 model somewhat underestimates the wind column density and thereby the Fe line strengths (Figure 5(a)). When the wind parameters were allowed to vary, the chi-squared value was significantly reduced from $\chi^2/{\rm dof} = 1406/1234$ to $1343/1231$ and the discrepancy between the data and model was mitigated (Figure 5(b)). The best-fit absorption model gives $N_H = 2.6^{+0.8}_{-2.1} \times 10^{22}$ cm^{-2}, $\xi = 8.8^{+0.5}_{-0.3} \times 10^4$ erg cm s^{-1}, and $v_{\rm wind} < 2 \times 10^2$ km s^{-1}. Thus, the thermal wind model can again explain, within a factor of ∼2, the absorption features in the high/soft state spectrum with a very weak hard tail.

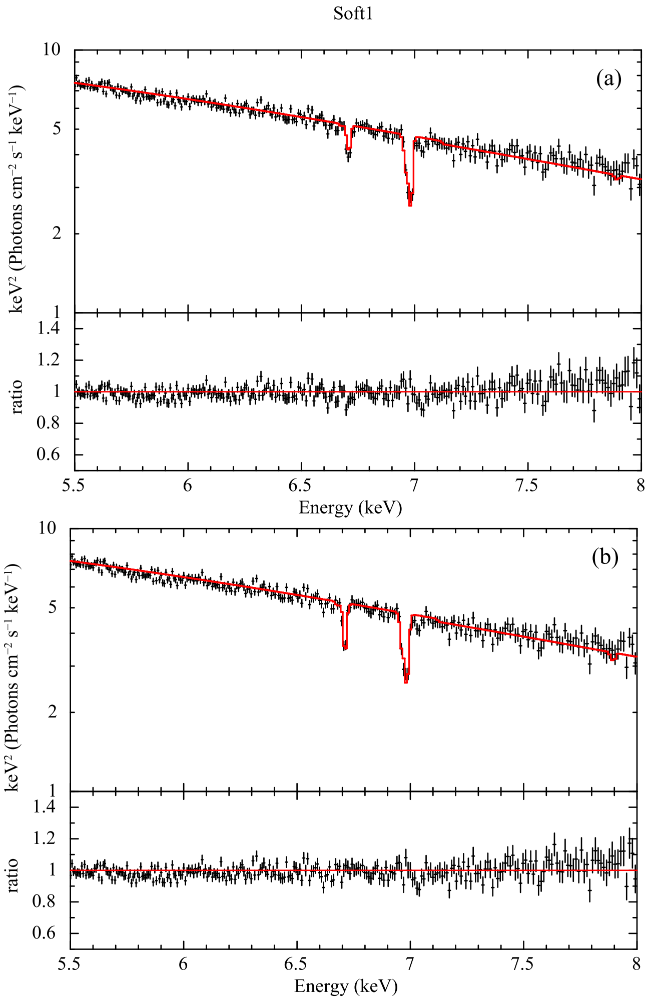

Figure 4. Comparison between the *Chandra* HETGS unfolded data at Soft1 and simulated absorption line spectrum based on the D18 model. The best-fit model obtained in Section 3 was adopted as the continuum model. (a) $N_{\rm H}$ and ξ are fixed at the value predicted by the wind model (see Table 2). (b) The best-fit model obtained by by allowing $N_{\rm H}$, ξ, and $v_{\rm out}$ to vary (see text). The lower panels present the data vs. model ratios.

5.2. Low/Hard State (Hard1 and Hard2)

Figure 6 shows the same sequence of fits to the *Chandra* data at Hard1. The upper panel shows the predicted absorption spectrum for the wind parameters fixed at the predicted values in Table 2. There are no significant features, which matches well to the observed data. The lower panel shows the resulting wind scaled in the same way as the best fit to Soft1 in the high/soft state; i.e., we reduce the column density and ionization parameter by a factor of two from the model predictions, but the wind is still not visible. We note that

---

[4] https://heasarc.gsfc.nasa.gov/xstar/docs/html/xstarmanual.html

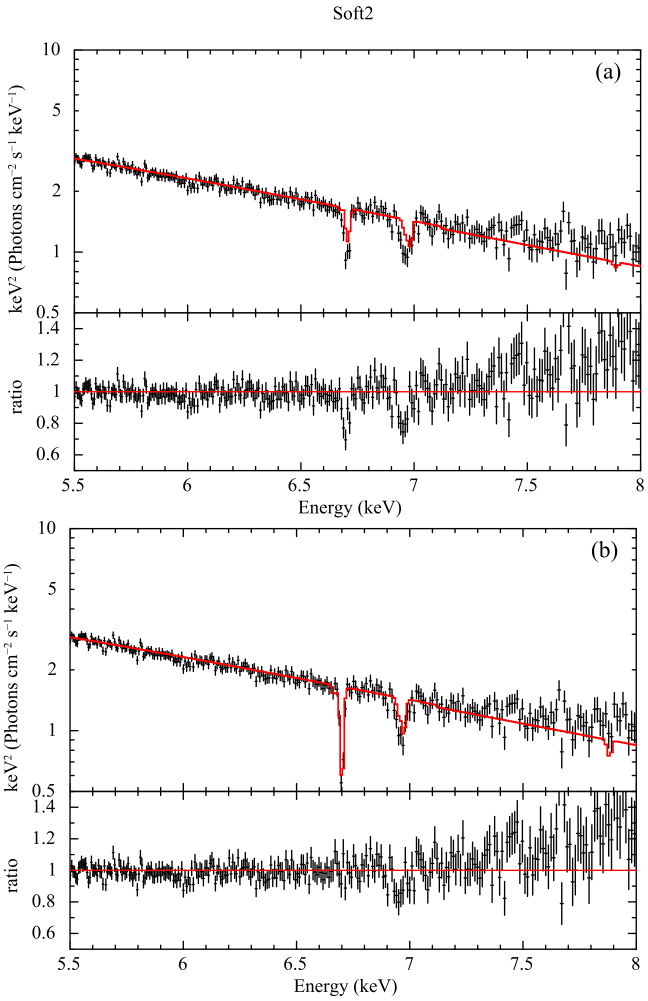

Figure 5. Same as Figure 4, but for the high/soft state data at Soft2.

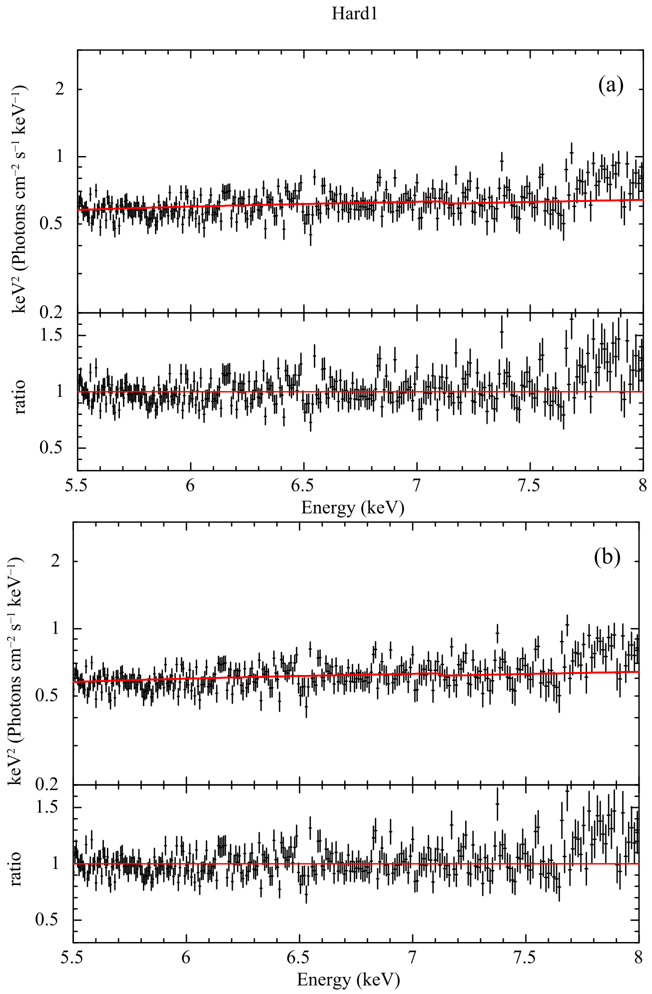

Figure 6. Same as Figure 4, but for the low/hard state data at Hard1, where (a) $N_{\rm H}$ and ξ are fixed at the value predicted by the wind model and (b) a factor of two smaller values are adopted.

the result unchanged even when we increase the column by a factor of two following the fit to Soft2.

Thus thermal wind model tailored to the observed luminosity and SED predicts no significant Fe K absorption lines in the low/hard state, which is consistent with the *Chandra* observation. This does not mean that the wind has disappeared. The simple thermal wind models predict that this lower luminosity spectrum should have a column which is only a factor of three smaller than that seen in the high/soft state. However, the higher $T_{\rm IC}$ means that the wind is now launched from much closer in. The ionization state is higher so the column of Fe XXV and even Fe XXVI is too small to be observed. The wind not only responds via photoionization to the changing spectral shape (see e.g., Chakravorty et al. 2013), but also responds in terms of its launch radius, velocity and density due to the change in Compton temperature.

This is similar to the conclusion of D18, though they had an inferred $L/L_{\rm Edd} = 0.02$ due to the difference in distance/mass/spin, rather than the $L/L_{\rm Edd} = 0.06$ determined here at these different system parameters. This is a bright/low hard state seen on the fast rise, where the transition to the high/soft state can occur at much higher $L/L_{\rm Edd}$ than the typical transition value of $0.02L_{\rm Edd}$ seen on the slow decline (hysteresis). Our estimate of $N_{\rm H} \sim 2.6 \times 10^{22}$ cm^{-2} is higher than the $N_{\rm H} = 1.8 \times 10^{22}$ cm^{-2} of D18 for these data, as the higher source luminosity is more than offsetting the effect of a smaller outer disk radius.

In Figure 7 we also show the HETGS spectrum around 7 keV obtained at Hard2 in 2015, where the source was a factor of ~2 fainter than Hard1 (i.e., $L/L_{\rm Edd} \sim 0.03$). No significant lines are visible, like Hard1. Although this epoch is out of the coverage of our calculation with D18 model, the wind parameters should be almost the same as those of Hard1, considering the only factor-of-two difference in flux. Our prediction is hence no lines in this fainter low/hard state, which is again consistent with the observation.

5.3. Very High State

Figure 8 makes a comparison of the VHS data in the very high state and the corresponding XSTAR simulation result, in the same manner as the other epochs. The HETGS spectrum shows no significant lines, although there may be a hint of a weak Fe XXVI line at 7 keV (see Figure 8(c)). Using D18 model we obtained a large wind column, 1.2×10^{23} cm^{-2}, and a moderate ionization parameter, 8.5×10^{4} erg cm s^{-1}, and thus our XSTAR simulation predicts significant detection of the Fe XXVI line, which is inconsistent with the observation. This discrepancy is not changed even if we consider the

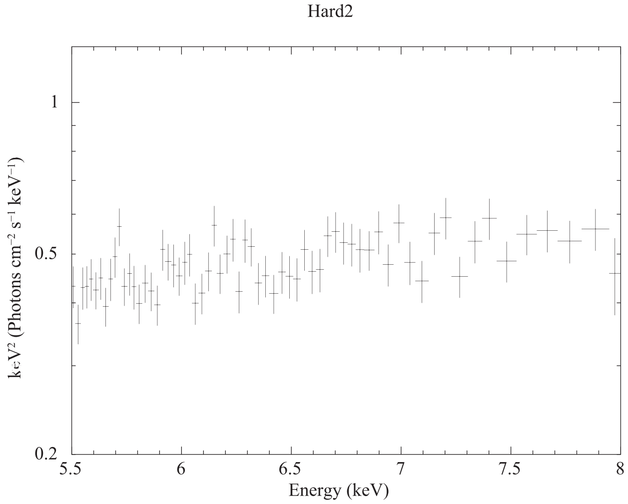

Figure 7. *Chandra* HETGS spectrum around 7 keV at Hard2. Data from three observations are coadded to improve statistics (see Table 1 for more details). A power-law model with a photon index of 1.3 was used to plot the unfolded spectrum.

factor-of-two uncertainty in the wind parameters found in the high/soft state.

Instead, we consider the more detailed thermal wind structure derived by Begelman & McKee (1983; see also Ostriker et al. 1991; Tomaru et al. 2019). These papers analyze the vertical structure of the X-ray irradiated upper layer of the disk. In the original paper of Begelman et al. (1983), the Compton heated material forms a static atmosphere over the inner disk. It is very easy for this to go optically thick in directions along the equatorial plane, shielding the outer disk from illumination until the convex disk shape brings the disk surface out of the shadow. Tomaru et al. (2019) show that this first directly illuminated point on the outer disk is almost exactly at $R_{\rm out}$ for the high/soft state of H 1743−322 (Soft1). We use their equations for the very high state parameters here and find that the higher Compton temperature means that the inner atmosphere has a larger scale height, so it casts a longer shadow, shielding the disk from direct irradiation across its entire extent (out to $1.4R_{\rm out}$). The precise suppression of illuminating flux depends on the detailed vertical structure of the inner disk atmosphere and X-ray corona geometry in this state, but the wind properties give a potential observable diagnostic of these poorly known quantities.

6. Discussion and Conclusions

Using the D18 model and X-ray data of H1743−322, we have investigated how thermal winds should evolve over an entire period of an outburst. The high cadence and the wide energy coverage of *RXTE* and *Swift*/BAT enabled us to accurately estimate the Compton temperature $T_{\rm IC}$ across all the outbursts. These broadband spectra then enabled us to predict the observable parameters of thermal winds throughout the outburst cycles.

We also make detailed photoionization models of the predicted thermal winds to compare with *Chandra* high-resolution spectral epochs. These match very well to the observed properties of the wind in the high/soft state data at ~30% $L_{\rm Edd}$ (Soft1) and at ~20% $L_{\rm Edd}$ (Soft2). The $N_{\rm H}$ and ξ values derived directly from the D18 model differ only by a factor of ~2 from the best-fit result. This strongly suggests that the thermal driving is the main launching mechanism of the observed wind, at least in this state. There is very little room in the data for any substantial contribution from a magnetic wind.

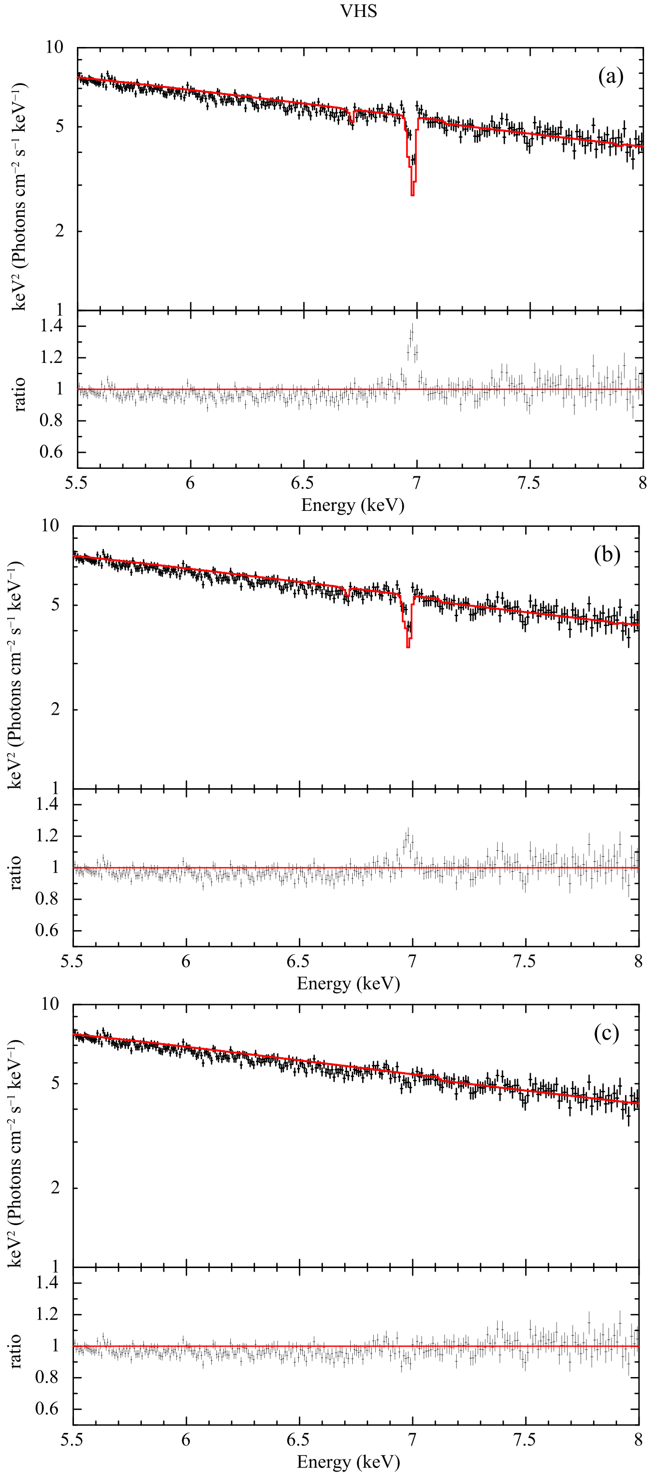

Figure 8. Same as Figure 4, but for the data at VHS, where (a) $N_{\rm H}$ and ξ are fixed at the value predicted by the wind model, (b) a factor of two smaller values are adopted. The unfolded spectra made with XSPEC are model-dependent and panel (a) and (b) are actually affected by the adopted absorption line models. To avoid this effect, panel (c) presents the unfolded spectrum to which only continuum model is applied.

The corresponding prediction for the bright low/hard state at 3%–6% $L_{\rm Edd}$ is that the absorption lines should not be visible, and this is again consistent with the *Chandra* data. The models predict that the harder spectrum can launch a wind from closer in, so even though the predicted column decrease is only a factor of three, its typical ionization parameter is increased by a large factor, especially when considering only the ionization of the iron species. These are controlled by X-rays above ∼8 keV where the difference in ξ becomes much larger than that estimated from the bolometric luminosity. In the high/soft state, the X-ray flux is dominated by the direct disk component below ∼10 keV, and the contribution of the hard tail is only ∼7% in the total luminosity at Soft1 and ∼0.2% at Soft2, whereas in the low/hard state, the hard X-rays above 8 keV contributes ∼75%. Thus, the ionization parameter for the ionization of iron is about 30–1000 times higher, and iron is almost completely ionized in the low/hard state.

Even though our predicted column is not visible even with *Chandra* in the low/hard state, it is still an overestimate of the spectral features, as the inner disk heated atmosphere can shield the outer disk from illumination (Begelman & McKee 1983; Tomaru et al. 2019). The larger scale height of this inner disk atmosphere leads to an increased shadow across the outer disk, predicting even lower wind mass-loss rates in the low/hard state (Tomaru et al. 2019).

We may be seeing evidence of this shadow at highest luminosities, during the very high state. Wind models without the shadow predict that the highest column density should be seen in these intermediate hardness spectra (turquoise points in Figure 3). The VHS *Chandra* data are close to this branch, and the photoionization simulations of the column and ionization state predicted by the simple thermal models of D18 give features which should be easily observable in the data, yet are not detected. We note, however, that the estimated wind parameters above 30%–40% L_{Edd}, where the radiation pressure effect plays an important role, may include an additional large systematic error, because our radiation pressure correction is only a simple approximation; we only considered the decrease of the wind launching radius, but the density and velocity structures would also change as well (D18, Tomaru et al. 2019), which is ignored in our assumption.

Our calculation using the D18 model is based on simple assumptions, and contains uncertainties caused by the system parameters including the disk size, the black hole mass, inclination, and the distance, the geometry (and hence illumination as a function of angle) of the X-ray source, and shape of the streamlines in the thermal wind, especially at high luminosities. All of these can affect the results, even though the Compton temperature was directly estimated from the actual X-ray spectra. More precise models require better determination of the system parameters, coupled to full radiation hydrodynamics to calculate the two-dimensional structure of the wind streamlines, followed by detailed radiation transfer to produce the spectral features (Tomaru et al. 2019). Nonetheless, even our simplified thermal wind model can already explain the observed behavior of the absorption lines in the low/hard and high/soft states. There is very little room for a strong magnetic wind which is not completely ionized in these data. Thermal winds do, however, overpredict the lines in the very high state. While this could be some form of magnetic suppression of the wind (Waters & Proga 2018), it seems more likely that this is due to an increasing scale height of the inner disk atmosphere reducing X-ray irradiation of the outer disk, where the thermal winds are launched. The wind features (or lack of them) could then give insight into the poorly constrained vertical structure of the X-ray source and X-ray illuminated inner accretion disk.

We thank the anonymous referee for providing valuable comments. M.S. acknowledges support by the Special Postdoctoral Researchers Program at RIKEN. This work is partly supported by a Grant-in-Aid for Young Scientists (B) 16K17672 (MS). This research has made use of MAXI data provided by RIKEN, JAXA and the MAXI team and *Swift* data supplied by the UK Swift Science Data Centre at the University of Leicester. C.D. acknowledges the Science and Technology Facilities Council (STFC) through grant ST/P000541/1 for support.

Facilities: RXTE (PCA and HEXTE), *Swift* (BAT), *Chandra* (HETGS).

Software: XSPEC (v12.9.0n; Arnaud 1996), HEAsoft (v6.19; HEASARC 2014), XSTAR (v2.41; on Astrophysics Source Code Library, Kallman & Bautista 2001).

References

Allen, J. L., Schulz, N. S., Homan, J., et al. 2018, ApJ, 861, 26

Arnaud, K. A. 1996, in ASP Conf. Ser. 101, Astronomical Data Analysis Software and Systems V, ed. G. H. Jacoby & J. Barnes (San Francisco, CA: ASP), 17

Begelman, M. C., & McKee, C. F. 1983, ApJ, 271, 89

Begelman, M. C., McKee, C. F., & Shields, G. A. 1983, ApJ, 271, 70

Bradt, H. V., Rothschild, R. E., & Swank, J. H. 1993, A&AS, 97, 355

Capitanio, F., Belloni, T., Del Santo, M., et al. 2009, ApJ, 398, 1194

Chakravorty, S., Lee, J., & Neilsen, J. 2013, MNRAS, 436, 560

Coriat, M., Fender, R. P., & Dubus, G. 2012, MNRAS, 414, 1991

Díaz Trigo, M., & Boirin, L. 2013, AcPol, 53, 659

Díaz Trigo, M., & Boirin, L. 2016, AN, 337, 368

Díaz Trigo, M., Migliari, S., Miller-Jones, J. C. A., & Guainazzi, M. 2014, A&A, 571, 76

Done, C. 2010, arXiv:1008.2287

Done, C., Tomaru, R., & Takahashi, T. 2017, MNRAS, 473, 838

Fukumura, K., Kazanas, D., Shrader, C., et al. 2017, NatAs, 1, 0062

Fukumura, K., Tombesi, F., Kazanas, D., et al. 2014, ApJ, 780, 120

Higginbottom, N., Proga, D., Knigge, C., et al. 2014, ApJ, 789, 19

Hori, T., Ueda, Y., Done, C., Shidatsu, M., & Kubota, A. 2018, ApJ, 869, 183

Huenemoerder, D. P., Mitschang, A., Dewey, D., et al. 2011, AJ, 141, 129

Ingram, A., Done, C., & Fragile, P. C. 2009, MNRAS, 397, 1

Kallman, T., & Bautista, M. 2001, ApJS, 133, 221

Kaluzienski, L. J., & Holt, S. S. 1977, IAU Circ., 3099, 3

Kotani, T., Ebisawa, K., Dotani, T., et al. 2000, ApJ, 539, 413

Kubota, A., Dotani, T., Cottam, J., et al. 2007, PASJ, 59, 185

Mahmoud, R. D., Done, C., & De Marco, B. 2019, MNRAS, 486, 2137

Makishima, K., Takahashi, H., Yamada, S., et al. 2008, PASJ, 60, 585

Miller, J. M., Raymond, J., Fabian, A. C., et al. 2006a, Natur, 441, 953

Miller, J. M., Raymond, J., Fabian, A. C., et al. 2012, ApJL, 759, 6

Miller, J. M., Raymond, J., Homan, J., et al. 2006b, ApJ, 646, 394

Miller, J. M., Raymond, J., Reynolds, C. S., et al. 2008, ApJ, 680, 1359

Mitsuda, K., Inoue, H., Koyama, K., et al. 1984, PASJ, 36, 741

Neilsen, J., & Lee, J. C. 2019, Natur, 458, 481

Neilsen, J., Rahoui, F., Homan, J., & Buxton, M. 2016, ApJ, 822, 20

Nomura, M., Ohsuga, K., Takahashi, H. R., Wada, K., & Yoshida, T. 2016, PASJ, 68, 16

Ostriker, E. C., McKee, C. F., & Klein, R. I. 1991, ApJ, 377, 593

Ponti, G., Fender, R. P., & Begelman, M. C. 2012, MNRAS, 422, L11

Proga, D., & Kallman, T. R. 2002, ApJ, 565, 455

Proga, D., Stone, J. M., & Kallman, T. R. 2000, ApJ, 543, 686

Shidatsu, M., Done, C., & Ueda, Y. 2016, ApJ, 823, 15

Shidatsu, M., Ueda, Y., Yamada, S., et al. 2014, ApJ, 789, 100

Steiner, J. F., McClintock, J. E., & Reid, M. J. 2012, ApJ, 745, 7

Steiner, J. F., Narayan, R., McClintock, J. E., & Ebisawa, K. 2009, PASP, 121, 1279

Tomaru, R., Done, C., Ohsuga, K., Nomura, M., & Takahashi, T. 2019, MNRAS, in press

Ueda, Y., Asai, K., Yamaoka, K., Dotani, T., & Inoue, H. 2001, ApJL, 556, L87

Ueda, Y., Honda, K., Takahashi, H., et al. 2010, ApJ, 713, 257
Ueda, Y., Yamaoka, K., & Remillard, R. 2009, ApJ, 695, 888
Uttley, P., & Klein-Wolt, M. 2015, MNRAS, 451, 475
Waters, T., & Proga, D. 2018, MNRAS, 481, 2628
Wilms, J., Allen, A., & McCray, R. 2000, ApJ, 542, 914
Woods, D. T., Klein, R. I., Castor, J. I., McKee, C. F., & Bell, J. B. 1996, ApJ, 461, 767
Yamada, S., Makishima, K., Done, S., et al. 2013, PASJ, 65, 80